LNOI Wireless Switches Based on Optical Phased Arrays for On-Chip Communication

Muhammad Khalid, Simone Ferraresi, Gaetano Bellanca, Marina Barbiroli, Franco Fuschini,
Velio Tralli, *Senior Member, IEEE*, Davide Bertozzi, Vincenzo Petruzzelli,
and Giovanna Calò, *Member, IEEE*

Abstract— **On-chip optical wireless links are attracting a great deal of interest as they can provide a possible solution to overcome the drawbacks associated with wired connections. In this paper, we propose a new approach for on-chip communication using optical wireless switches based on thin-film lithium niobate on insulator (LNOI) technology. The optical wireless switches exploit reconfigurable optical phased arrays (OPAs) both at the transmitter and at the receivers. We investigate the radiation characteristics and design criteria of the LN antenna element serving as a unit radiator in the OPAs. We then demonstrate the implementation of an on-chip optical wireless switch in a simple infinite homogeneous host medium and assuming a realistic multilayer structure configuration. Moreover, we examine the impact of various geometrical parameters and the fabrication imperfections on the device performance and provide a discussion on the design optimization. Our findings assess the feasibility of optical wireless switches based on LNOI technology for on-chip wireless communication.**

Index Terms— **Optical wireless switches, on-chip communication, optical phased arrays, LNOI technology.**

I. INTRODUCTION

IN THE last few years there has been a surge of interest in integrated Optical Phased Arrays (OPAs) due to their outstanding capabilities of dynamically controlling light for classical and quantum communication [1], [2], [3], [4]. OPAs are actively being explored as they gain momentum in a wide range of application domains ranging from low-cost LiDAR (Light Detection and Ranging) on autonomous vehicles [5], [6] to lens-less imaging [7], augmented reality and biophotonics [8], [9].

Commercially available OPAs are bulky, power-hungry and require mechanical means (such as motor-driven rotating mirrors) for beam steering which limit the switching speed and degrade the device efficiency [10]. Integrated OPAs have been developed as a low-power, robust, reconfigurable and scalable beam steering platform [11], [12], [13]. Beam steering in OPAs is achieved by changing the phase profile of the beam via optical phase shifters, mostly based on the thermo-optic (TO) or electro-optic (EO) effects. TO effect is obtained by heating electrodes to phase shift the propagating signal by changing the material refractive index [14], [15], [16]. EO effect is achieved by applying an external bias voltage to change the refractive index of the material [17], [18]. Integrated OPAs, owing to their non-mechanical beam steering capability, have been proposed as basic building blocks for on-chip optical wireless networks [19]. Their potential for innovation and optimization in this domain is significant due to the severe limitations of wired optical links and crossbars in terms of layout complexity, power losses, latency and scalability [20], [21], [22]. In contrast, on-chip wireless communications hold promise of more performance- and energy-efficient data transfers through more compact devices. A significant research in this domain has been witnessed recently, using various fabrication platforms based on different materials and technologies, and on different frequency ranges extending from THz to optical frequencies [23], [24], [25].

The optical domain offers the advantage of mature fabrication technologies which are integrable with electronic layers. Among various optical platforms, Silicon on Insulator (SOI) technology is one of the most commonly used for integrated photonic components. It has also facilitated the integration of SOI waveguides with dielectric or plasmonic nanoantennas that opened up a broad spectrum of applications ranging from OPA LiDARs to selective nanotweezers [26], [27], [28], [29]. Nonetheless, the non-negligible propagation losses and power consumption of SOI components often limit the scalability of integrated photonic circuits [30], [31]. In order to address the shortcomings of the Si platform, silicon nitride (SiN) and SiN-Si hybrid integration emerged as alternatives, resulting in remarkable progress in improving the performance of photonic devices [32]. However, these platforms have their own limitations, for example, low thermo-optic coefficient and fabrication

complexity, which hinder their applications in many fields, especially when reconfigurability is required.

Recently, the introduction of thin-film Lithium Niobate (LN) has sparked extensive research in the field of integrated photonics. LN is considered as one of the most suitable materials for photonic integrated circuits by virtue of its high intrinsic EO and TO effects [18], [33], strong second-order nonlinearities for on-chip frequency conversion [34], large optical transparency window, low material losses [35] and piezo-electric properties [36]. Lithium Niobate on Insulator (LNOI) technology involves the fabrication of thin-film LN on an insulator, and being compatible with the CMOS technology [37], integration process of LNOI-based devices can follow the same procedure as that adopted in the case of SOI technology. For example, one promising possibility could be the monolithic integration, as has been successfully demonstrated for integrated OPAs using standard SOI CMOS process [38], [39]. Another possibility could be employing potentially simpler approach, similar to one reported in [40], using a chiplet assembly with 3D-staking on a photonics interposer.

LNOI technology has a potential to revolutionize the LN industry as it enables exploiting interesting characteristics of LN to design and fabricate innovative photonic devices, while concurrently achieving fast modulation, low-power consumption, low optical loss and high integration density [16], [41], [42]. LNOI technology has remarkable advantages over the other existing fabrication techniques in terms of device scalability, performance and power saving. Performance and scalability are intrinsically limited by insertion loss and crosstalk. The LNOI technology offers the possibility of realizing integrated devices with much-reduced footprints. Smaller footprint means a significant increase in the scalability, for example, a commercially available 6-in LNOI wafer can accommodate as many as 3000 EO modulators [33]. Scaling up an optical switching device comes at the cost of higher losses (as each switch introduces an insertion loss) and increased footprint. Since the proposed optical switches are based on OPAs, they offer a possibility of addressing more receivers by increasing the number of radiating antennas. A different choice, without increasing the number of antennas, could be widening the interspacing between the radiating units of the OPAs. Increasing the distance between the radiators results in grating lobes, which can be exploited to address more receivers.

Thin-film lithium niobate (TFLN) is an emerging platform with a relatively brief history. Despite being in its infant stage, the overall performance of these devices is already on par with, if not exceeding, the performance of other well-established material platforms which have benefitted from decades of research and development. While Si lacks the intrinsic EO effect, LN has a very large EO coefficient, allowing realization of high-speed photonic devices. For instance, integrated LN modulators with a 3 dB bandwidth beyond 100 GHz and with data rates up to 240 Gbit/s have been demonstrated [43], paving the way for realization of high-speed OPAs. Furthermore, propagation losses in LN waveguides can be minimized close to 0.0034 dB/cm [44], providing a substantial advantage as compared to Si and InP. Microresonators utilizing the LNOI platform with record high quality factor of the order of 10^8 have been successfully demonstrated [45]. A comparison between the Mach-Zehnder interferometer (MZI)- and microring resonator (MRR)-based optical switches in LNOI technology shows a similar switching speed as compared to SOI and Si_3N_4 platforms but with considerable smaller footprint and insertion loss [46]. In a recent study [47], a performance comparison of LN OPAs with other platforms including Si and InP has been reported. It has been demonstrated that performance of LN OPAs is much higher than those based on other material platforms. In [47] a bandwidth up to 2.5 GHz was achieved in the LN OPAs, resulting at the level of MHz in other platforms. LN OPAs have lower power consumption (0.33 nJ/π) and higher field of view ($50° \times 8.6°$) as compared to other technologies. Similarly, another recent study reports a performance comparison of LN OPAs with other technologies, reporting a low power consumption (1.11 nJ/π), a fast operation speed (14.4 ns) and a large field of view ($62.2° \times 8.8°$) in LNOI technology [48]. The reader seeking additional information may refer to this literatures [43], [44], [45], [46], [47], [48], and [49].

In this paper, we propose a new approach to on-chip communication which aims at combining the advantages of lithium niobate, such as low power consumption, fast response time, etc., with the reconfigurability and wide-band operation of the on-chip wireless networks. The demonstration of the feasibility of LNOI technology for on-chip wireless communication can pave the way for new avenues in network design exploration. In particular, here we propose an on-chip optical wireless switch based on reconfigurable OPAs realized in LNOI technology. In order to demonstrate the feasibility of on-chip wireless communication, we study the design and radiation characteristic of LN taper antennas, used as basic radiators in the OPAs. We then propose the design of an optical wireless switch for on-chip communication. We consider that the optical switch, composed of transmitting and receiving OPAs, is based on LNOI technology. Numerical implementation of the on-chip wireless switch has been carried out by assuming at first a simple case of an infinite homogeneous host medium, and then by considering an on-chip multilayer structure, which is representative of a realistic scenario in the LNOI fabrication. We also discuss the effect of multipath propagation originating from the multiple reflections at the interfaces of the layered media. The performance of the device in terms of insertion loss and crosstalk has been evaluated employing three-dimensional finite-difference-time-domain (FDTD) method. Additionally, we present a statistical analysis of the impact of fabrication imperfections on the performance of OPAs.

II. WIRELESS SWITCH: OPERATION PRINCIPLE

On-chip optical switches are crucial components of integrated photonic devices for enabling reconfigurable signal routing and processing. These switches have a wide range of potential applications in optical communications and networks, biosensing, photonic computing and data centers [17], [50], [51]. In optical networks, these wireless switches can be used for broadband reconfigurable on-chip communication. They can be employed to transmit optical signals using wavelength division multiplexing, enabling parallel transmission of various
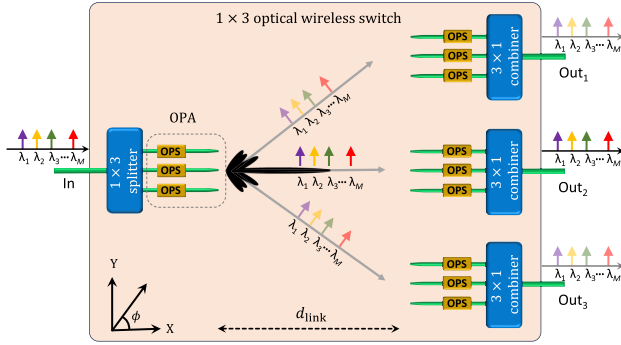
Fig. 1.   Schematic representation of the 1×3 optical wireless switch based on reconfigurable optical phased arrays (OPAs). Each OPA consists of $N_a = 3$ antennas and the phase shift in each antenna is governed by optical phase shifters (OPS). By properly choosing the phase shift the transmitter can address one of the receivers at the output. M different wavelengths λ_i ($i = 1, 2, 3, \ldots, M$) can be transmitted contemporarily using the wavelength division multiplexing scheme.
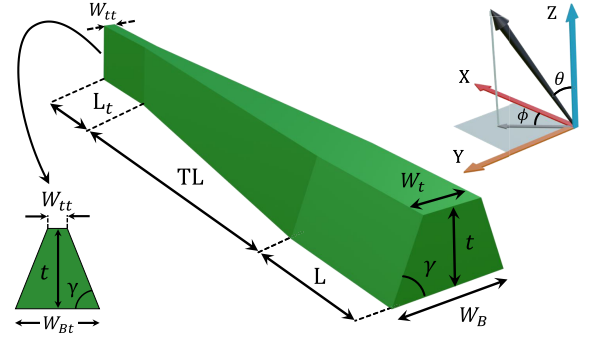

Fig. 2.   Schematic view of LN antenna element used as a radiator in the design of optical phased arrays. The antenna consists of an input straight waveguide of length L, an inversely tapered waveguide of length TL, and a taper tip constructed by a narrow straight waveguide of length L_t. The input waveguide has a top width W_t, thickness t, sidewall angle γ and base width W_B. The tip of the antenna has a top width W_{tt} and base width W_{Bt}. It is considered that the antenna is immersed in silica with refractive index $n_{SiO_2} = 1.445$.

data channels, and to improve the interconnection between different processing units in densely integrated computing architectures [12], [19].

Majority of the conventional structure-designs of on-chip optical switches are based on the MRR or MZI [17], [46]. MRR switches have the advantage of smaller size and low power consumption, but they have limited bandwidth due to their resonant behavior and are sensitive to fabrication errors and temperature changes. MZI-based switches, on the other hand, have large working bandwidth and fast switching speed, however, they have high insertion losses and crosstalk [52]. Optical wireless switches have several advantages over wire-based optical switches. For example, they are more energy efficient, reliable and enable improved scalability. On-chip wireless switches are in their early stage of research and their potential has not been fully explored yet. Nonetheless, they hold a great promise for providing high speed, low insertion loss and low power consumption. These wireless switches present a favorable alternative to MZI- and MRR-based switches, particularly when reconfigurability is crucial. Furthermore, owing to their non-resonant behavior, optical wireless switches do not need extreme fine tuning, unlike in the MRR-networks.

In this section, we discuss the design and radiation characteristics of the LN taper antenna and the OPA, used as basic building blocks in the implementation of the optical wireless switch. A schematic representation of the 1×3 optical wireless switch based on reconfigurable OPAs is shown in Fig. 1. Each OPA consists of $N_a = 3$ antennas and the phase shift in each antenna is governed by optical phase shifters (OPS). By properly choosing the phase shift the transmitter can address one of the receivers at the output.

As shown in Fig. 1, the transmitting node consists of power splitters, OPS and OPAs made by taper antennas for the radiation. Similarly, the receiving nodes are made up of receiving OPAs, OPS and power combiners. It is worth underlining that the proposed analysis focuses on the design of the switch and of the OPAs, whereas the other components are out of the scope of the paper. Nonetheless, power splitting and combining can be achieved cascading multiple Y-branches or Multimode Interference (MMI) beam splitters/combiners. The

proposed 1×3 optical wireless switch can be used to address each of the three receivers by applying a suitable phase shift between the antenna elements. In order to establish a communication with a particular receiver, the beam steering can be achieved by changing the phase shift of the OPAs through optical phase shifters. Given the broadband behavior of the designed OPAs, the proposed device can be used to transmit M different wavelength channels λ_i ($i = 1, 2, 3, \ldots, M$) according to wavelength division multiplexing schemes.

A. Design and Characteristics of LN Taper Antenna

We report the design of a LN taper antenna with trapezoidal cross-section, used as a fundamental radiating element in the design of the on-chip wireless switch. The trapezoidal cross section (slanted sidewalls) of the LN antenna is a common feature observed in fabricated LN waveguides. This is due to fabrication imperfections originating from the complex nature of the etching processes involved [35], [53]. The geometry of the antenna element, as shown in Fig. 2, consists of an input straight waveguide of length L, an inversely tapered waveguide of length TL, and a taper tip constructed by a narrow straight waveguide of length L_t. The antenna element has a thickness t and a sidewall angle γ, which are considered constant along the structure. The input waveguide has a top width W_t and a base width W_B, whereas, the tip of the antenna has a top width W_{tt} and a base width W_{Bt}. The front view of the taper tip is depicted in the inset of Fig. 2. In our analysis, we consider an X-cut LN crystal with the optical axis aligned with the Y-axis of the Cartesian coordinate system (see Fig. 2). We also include wavelength dispersion and material anisotropy of LN in our numerical model, and represent the refractive index n_{LN} in the matrix form, as:

$$n_{LN} = \begin{pmatrix} n_o & 0 & 0 \\ 0 & n_e & 0 \\ 0 & 0 & n_o \end{pmatrix} \qquad (1)$$

where n_o and n_e indicate the ordinary and extra-ordinary refractive indices, respectively. Furthermore, we consider that the designed antenna operates in the C-band of the telecommunication frequencies.
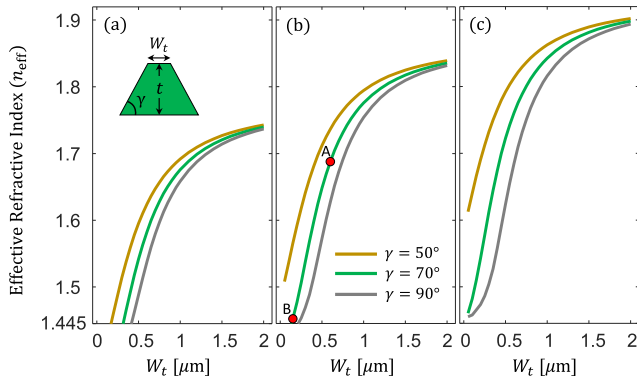
Fig. 3. Effective refractive index n_{eff} as a function of waveguide top width W_t for different values of the sidewall angle γ, considering the waveguide thickness (a) $t = 300$ nm, (b) $t = 400$ nm and (c) $t = 500$ nm. The LN waveguide is immersed in silica (SiO_2) with $n_{\text{SiO}_2} = 1.445$ at the free-space wavelength $\lambda = 1.55$ μm. The red circles A and B in (b) correspond to the top width of the input waveguide and of the taper tip, respectively, considered in the present analysis.

In order to design the antenna, we first analyze the fundamental transverse-electric mode of the LN trapezoidal waveguide immersed in silica (SiO_2) with refractive index $n_{\text{SiO}_2} = 1.445$ at the free-space wavelength $\lambda = 1.55$ μm. In Fig. 3, the effective refractive index n_{eff} is computed as a function of the waveguide top width W_t for different values of the sidewall angle γ and the waveguide thickness t. It can be observed that n_{eff} shows a strong dependence on the geometrical parameters of the waveguide. In particular, for smaller sidewall angles γ, the effective mode index tends to increase. This is because a smaller value of γ corresponds to a larger base width W_B (for a given W_t, $W_B = W_t + 2t/\tan\gamma$), and thus providing a better mode confinement in the waveguide. Similarly, as can be seen from Figs. 3 (a)-(c), an increment in the waveguide thickness t and top width W_t, increases the effective mode index n_{eff}, resulting in an enhanced mode confinement.

For an efficient radiation, the taper should transform a propagating mode at the input waveguide into an evanescent mode at the taper tip. This can be achieved by choosing the tip width W_{tt} close to the cut-off condition. Looking at the results of Fig. 3, different geometrical configurations can be chosen to achieve the required condition. As an example, we have selected a waveguide with thickness $t = 400$ nm and sidewall angle $\gamma = 70°$. The input waveguide width is chosen equal to $W_t = 600$ nm, as denoted by the red circle A in Fig. 3 (b), to have a well-confined mode. The taper tip width is set to $W_{tt} = 150$ nm, as represented by the red circle B in Fig. 3 (b), corresponding to an evanescent mode (near the cut-off condition).

With the design parameters at hand, we study the radiation characteristics of the LN taper antenna. We simulate the antenna by the three-dimensional FDTD method [54]. The gain of the antenna, as a function of the azimuthal angle ϕ and the inclination angle θ at $\lambda = 1.55$ μm, is plotted in Fig. 4 (a) with $\gamma = 70°$, TL $= 2$ μm and L $= L_t = 1$ μm. The angle ϕ and θ are defined according to the spherical coordinate system (see inset of the Fig. 2). The gain in the azimuthal plane is plotted at $\theta = 90°$ and the gain in the inclination plane is plotted at $\phi = 0°$. It can be noticed that the maximum radiation gain
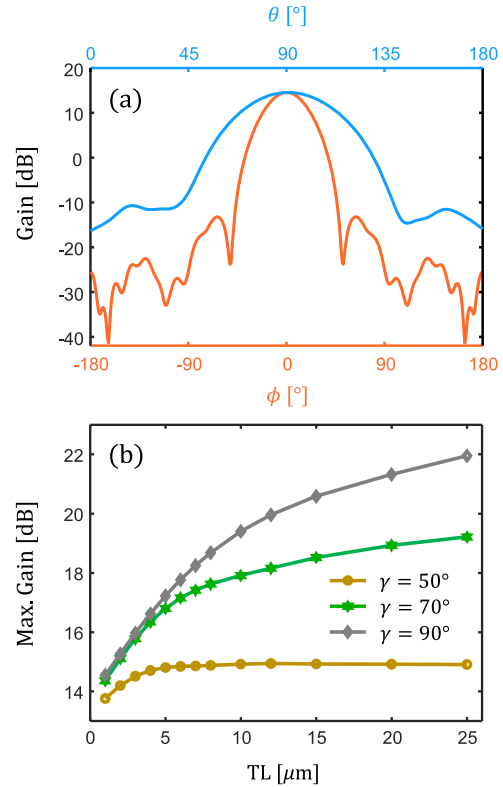

Fig. 4. (a) Radiation diagram of LN antenna at $\lambda = 1.55$ μm, in both the azimuthal plane (ϕ) and the inclination plane (θ), considering TL $= 2$ μm, L $= L_t = 1$ μm and $\gamma = 70°$. (b) Maximum Gain of the antenna as a function of TL plotted for different values of sidewall angle γ.

occurs at $\phi = 0°$ and $\theta = 90°$, which is the direction of the mode propagation, i.e., along the X-direction (see Fig. 2). The maximum gain of the antenna as a function of taper length TL is plotted in Fig. 4 (b) for different values of the sidewall angle γ. We observe that the gain of the antenna increases for longer taper lengths, and it is also strongly influenced by the sidewall angle γ. For smaller γ, the gain quickly converges to an asymptotic value as the taper length increases. For larger γ, the gain is higher and increases for the longer TL. Moreover, we have verified that the maximum gain of the antenna remains almost constant in the entire C-band frequencies (not shown).

B. LNOI Optical Phased Arrays

The LN antenna discussed in the previous section can serve as a radiator in the reconfigurable optical phased arrays. We consider here an OPA constructed from N_a identical LN taper antennas. Such OPA can be used as a building block in the design of optical wireless switches for on-chip interconnections. Therefore, we first examine the radiation properties of an OPA composed of an array of N_a identical antennas aligned along the Y-axis and separated by a distance d_a (defined as center-to-center distance between two adjacent waveguides). According to the antenna theory, the radiation pattern of an OPA can be obtained by multiplying the radiation diagram of a single antenna with an array factor (AF), defined as [55]:

$$\text{AF} = \sum_{q=1}^{N_a} b_q e^{-j(q-1)[kd_a\cos(\phi)+\alpha]} \tag{2}$$
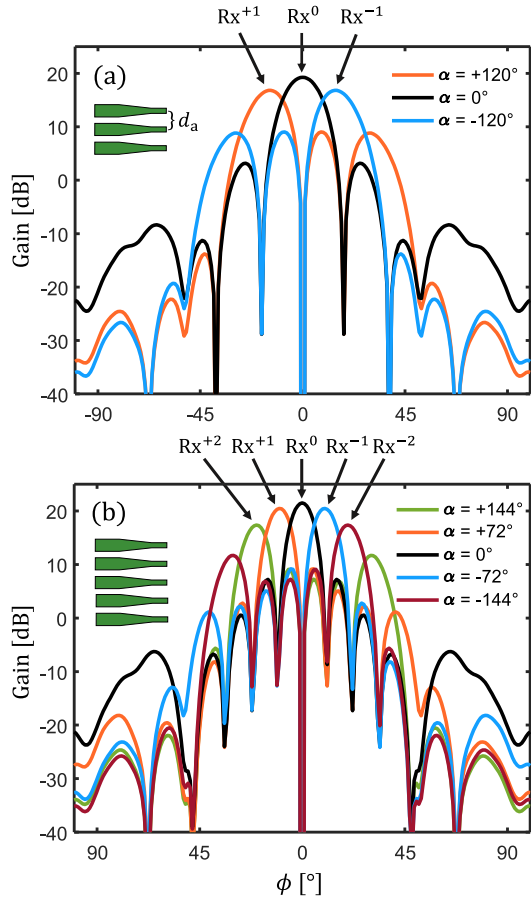
Fig. 5. Gain of an LN OPA made of (a) $N_a = 3$ and (b) $N_a = 5$ identical LN taper antennas as a function of the azimuthal angle ϕ at $\lambda = 1.55$ μm. The phase shift $\alpha = \pm 360°/N_a$ is applied between the antenna elements for beam steering to illuminate different receivers.

where b_q is the excitation amplitude of each antenna element, $k = 2\pi/\lambda_m$ is the propagation constant with the wavelength in the embedding medium $\lambda_m = \lambda/n_{SiO_2}$, and α is the phase difference of input signals applied between two adjacent antennas. For the sake of convenience, we assume $b_q = 1$ (uniform OPAs) throughout the paper, unless otherwise specified. Figure 5 shows the radiation diagram of an OPA with $N_a = 3$ and $N_a = 5$ as a function of azimuthal angle ϕ at $\lambda = 1.55$ μm. The number of main lobes in the radiation diagram depends on d_a, i.e., the distance between the two adjacent antenna elements. It is important to remark that the trapezoidal cross-section of the waveguide imposes a lower limit on d_a which must be greater than W_B (i.e., $d_a > W_B$). In the present analysis, as an example, we arbitrarily choose $d_a = W_B + \lambda_m/4 = 1.08\lambda_m \approx \lambda_m$, where $\lambda_m = \lambda/n_{SiO_2}$ is the wavelength in the cladding medium with free-space wavelength λ. For the chosen distance $d_a \approx \lambda_m$, only one main lobe exists in the radiation diagram [56]. The main radiation lobe can be steered in the XY−plane by applying a suitable phase difference α between the antenna elements comprising the OPA. The phase shifts can be obtained through optical phase shifters based on electro-optic or thermo-optic effect [57], [58].

The radiation pattern of the OPA with $N_a = 3$ is plotted in Fig. 5 (a) for different values of the phase difference

between the radiating antennas. As can be seen from the radiation diagram, when $\alpha = 0°$, i.e., the radiators comprising the OPA are all in phase, the gain pattern shows a single main lobe with its maximum at $\phi = 0°$. However, when $\alpha = \pm 360°/N_a = \pm 120°$, the maximum of the radiated beam can be steered in correspondence of the first nulls in the radiation diagram of the broadside OPA. This non-mechanical reconfigurability of the OPA can be utilized to steer a radiated beam for addressing different receivers, for example, three receivers in the present scenario (i.e., Rx^{+1}, Rx^0 and Rx^{-1}). Figure 5 (b) shows the radiation profile of the OPA with $N_a = 5$. From the radiation diagrams in Figs. 5 (a) and (b), it can be noticed that, as expected [12], by increasing the number of antennas increases the maximum gain and the number of zeros in the radiation diagram. These characteristics can be exploited to increase the number of addressable receivers. For example, according to Fig. 5 (b), five different receivers can be addressed when a suitable phase difference $\alpha = (0°, \pm 360°/N_a)$ is applied between the antenna elements. The non-addressed receivers can be positioned in accordance with the nulls of the broadside radiation diagram (i.e., $\alpha = 0°$) to minimize the crosstalk. These OPAs can be exploited to realize a broadband optical wireless switch for on-chip interconnections.

III. DESIGN OF A LNOI ON-CHIP WIRELESS SWITCH

In this section, we demonstrate the design of a LNOI optical wireless switch utilizing the OPA as a building block. We present a numerical analysis of the on-chip wireless links with reconfigurable switching functionality. As an example, we demonstrate an optical link comprising OPAs to construct 1×3 switching matrix in which a transmitter Tx can efficiently address one of the three in-plane receivers Rx^i ($i = 0, \pm 1$). First we consider the case in which each transmitting and receiving OPAs are composed of $N_a = 3$ LN taper antennas. The link distance between the transmitter and the broadside (Rx^0) receiver is d_{link}, and the distance between two adjacent receivers is Δy, as schematically shown in Fig. 6. The reconfigurability can be attained by applying a suitable phase difference α between the antenna elements of the OPAs.

A. Homogeneous Host Medium

In order to simplify the analysis, we initially examine a simplified case of study in which the transmitter and receivers are hosted by an infinite homogeneous medium with refractive index n_{SiO_2}. Using 3D-FDTD simulations, we compute the insertion loss (IL) for each receiving OPAs, and evaluate the crosstalk (XT) between the receivers. The insertion loss (IL) defined as [19]:

$$IL = -10 \log_{10}(T_i) \tag{3}$$

where T_i is the transmittance at the addressed receiver Rx^i ($i = 0, \pm 1$). The crosstalk ($XT_{i,j}$) between the addressed receiver Rx^i and non-addressed receiver Rx^j is expressed as:

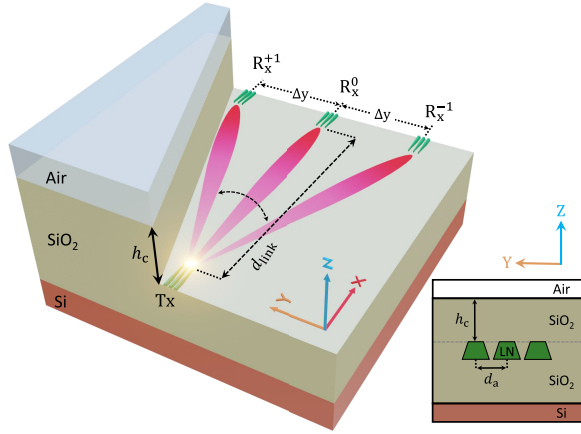$$XT_{i,j} = 10 \log_{10}\left(\frac{T_i}{T_j}\right) \tag{4}$$

Fig. 6. Schematic of 1×3 wireless switch based on OPAs, composed of $N_a = 3$ identical LN taper antennas. A transmitter Tx can address each of the three receivers Rx^i ($i = 0, \pm 1$), depending upon the phase difference $\alpha = 0°, \pm 360°/N_a$ between the radiators comprising OPAs. d_{link} is the distance between the transmitter and the broadside receiver ($\alpha = 0°$) and d_a is the center-to-center distance between two adjacent antenna elements of the OPAs. The separation between the two neighbouring receiving OPAs is Δy. The inset illustrates the cross-section in the YZ−plane at the input of the wireless switch, when also the multilayer structure is considered.

Fig. 7. Performance of a 1×3 wireless switch hosted in an infinite homogeneous medium. Left panel: Transmittance in dB computed at each receiving node at $\lambda = 1.55~\mu m$, by using 3D-FDTD simulations for different values of the phase shift (a) $\alpha = +120°$, (d) $\alpha = 0°$ and (e) $\alpha = -120°$. Right panel: The electric field ($|E|$) profile (in log scale) in the XY−plane showing beam steering to address different receivers depending upon the applied phase shifts between the antenna elements: (b) $\alpha = +120°$, (d) $\alpha = 0°$ and (f) $\alpha = -120°$. In these simulations, we consider $d_a \approx \lambda_m$ and $d_{link} = 70~\mu m$.

where T_j is the transmittance computed at the non-addressed receiver Rx^j, where $j = 0, \pm 1$ and $j \neq i$.

Figures 7 show the transmittance (Figs. 7 (a), (c) and (e)) as a function of the free-space wavelength λ, and the electric field ($|E|$) profiles (Figs. 7 (b), (d) and (f)) in the XY−plane (i.e., in the ϕ−plane) for different values of the input phase shifts. To obtain these results, we choose $d_a \approx \lambda_m$ ($= 1.08\lambda_m$) and an arbitrarily value for the link distance $d_{link} = 70~\mu m$. As shown in Fig. 7 (a), when the phase difference between the radiators is $\alpha = 0°$, the transmitter communicates with the central receiver Rx^0 with IL $= 18$ dB and $XT_{0,\pm 1} = -37$ dB. Similarly, when $\alpha = +120°$ (or $-120°$), the transmitter aims at the upper (or lower) receiver Rx^{+1} (or Rx^{-1}) with IL $= 21$ dB and the worst-case crosstalk is $XT_{1,0}$ (or $XT_{-1,0}$) $= -23.3$ dB, as shown in Fig. 7 (c) (or (e)). We have compared the computed IL for the broadside communication with the well-known Friis transmission equation [22], [59] and the results agree very well. Figures 7 (b), (d) and (f) show the electric field $|E|$ profiles in the XY−plane for $\alpha = +120°$, $\alpha = 0°$ and $\alpha = -120°$, respectively, demonstrating the beam steering to illuminate an assigned receiver. It is worth noting that, when the transmitter Tx aims at a specific receiver Rx^i ($i = 0, +1, -1$), the addressed receiver registers maximum power while the other non-addressed receivers Rx^j (where $j = 0, +1, -1$ and $j \neq i$) fall at radiation minima. For example, for $\alpha = 0°$ the transmitted beam with the main radiation lobe illuminates the broadside receiver Rx^0, whereas, the non-addressed upper Rx^{+1} and lower Rx^{-1} receivers get minimum signal. The received signal can be minimized by positioning the OPA receivers at a distance $\Delta y = d_{link} \tan(\Phi_{null})$. The angular position of the nulls Φ_{null}, corresponding to the minima in the radiation diagrams of Figs. 5, can be determined by the following relation [12]:

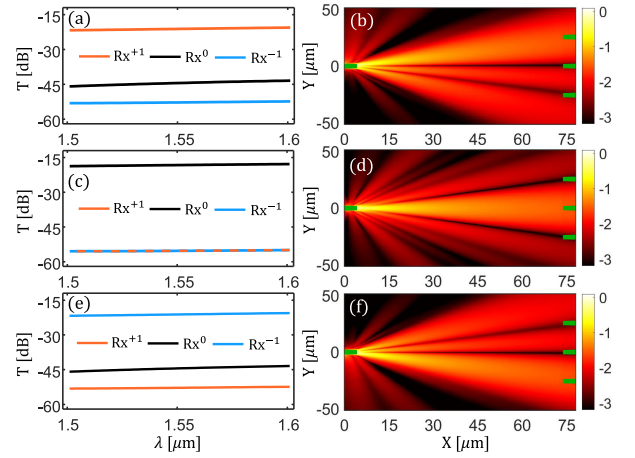$$\Phi_{null} = \pm \sin^{-1}\left(\frac{\lambda_m}{d_a N_a}\right) \quad (5)$$

which depends on the wavelength in the embedding medium λ_m, the distance between the radiators d_a and the number of antennas N_a comprising the OPAs.

B. Multilayer Structure Configuration

In integrated photonic devices, the structure configuration for on-chip communication is based on the multilayers of different materials. This typical LNOI multilayer configuration is common in commercial wafers [22], [60]. It consists of a bottom thick layer of bulk Si (or LN) superimposed by a thick silica layer, serving as a substrate to LN waveguides. The cladding layer, in general, is a polymer that is spin coated over the sample and, in the case of our optical wireless switch, it can be chosen to reduce the propagation loss of the wireless propagating signal.

The analysis conducted in the previous subsection, considering an infinite homogeneous host medium, is useful to define the design criteria and to understand the working principle of the 1×3 switch. However, it overlooks the multipath propagation effect originating from the medium discontinuities present in the on-chip optical wireless scenarios [22]. In the following, we consider the multilayer configuration which is typical of the fabricated samples in an on-chip communication scenario, as often studied in LNOI technology. The optical link is composed of a multilayer structure, as schematized in Fig. 6, consisting of a bottom bulk Si layer superimposed by a SiO_2 layer of thickness h_{sub}, acting as a substrate to the LN waveguide of thickness t. The LN waveguides are covered with a finite cladding layer of SiO_2 with thickness h_c interfacing with free space. We extract the geometrical and material parameters from the literatures [12], [22], and [60]. In our numerical model, we consider the bottom-most Si and the top-most air layers to be infinite by employing the perfectly matched layer boundary conditions. The thickness of substrate is taken as $h_{sub} = 3~\mu m$. In our analysis, we examine the behavior of LN waveguides with various thicknesses t ranging

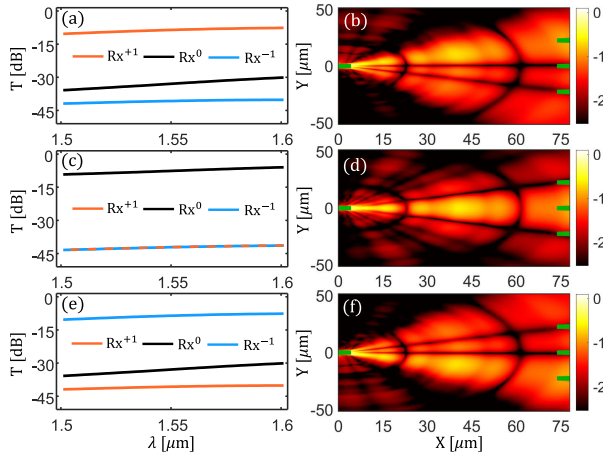Fig. 8. 1×3 optical wireless switch based on multilayer structure configuration. Left panel: Transmittance at each receiving OPAs for (a) $\alpha = +120°$, (c) $\alpha = 0°$ and (e) $\alpha = -120°$. Right panel: The electric field ($|E|$) profile in the $XY-$plane showing beam steering to address different receivers, considering (b) $\alpha = +120°$, (d) $\alpha = 0°$ and (f) $\alpha = -120°$. These results are obtained for $h_c = 3$ μm and $d_{\text{link}} = 70$ μm at $\lambda = 1.55$ μm.

from 0.3 μm to 0.5 μm, and of the cladding layer with thicknesses h_c ranging from 0.5 μm to 5 μm.

Propagation in multilayer structures gives rise to multiple reflections of the optical signals at the multiple interfaces which can induce an increase or decrease of the received power due to constructive or destructive interference. Careful choice of the chip layer structure can result in received signal with higher strength, as compared to the link operating in an infinite homogeneous medium. Considering SOI technology, a comparison showing a very good agreement between the FDTD simulations and experiments of a multilayer wireless link has already been reported [22]. It has been demonstrated that multipath phenomena induced by the multilayer structure can have a strong impact on the performance of the optical link, and can be exploited to improve the received power. Figure 8 shows the transmittance (Figs. 8 (a), (c) and (e)) and the electric field profiles (Figs. 8 (b), (d) and (f)) for the on-chip multilayer structure implementing a 1×3 wireless switch. It is interesting to note that, in this scenario, the received power at each targeted OPA is higher as compared to the case of propagation in homogeneous medium. When Tx aims at Rx^0 ($\alpha = 0°$) the insertion loss is $IL = 7.5$ dB and the crosstalk is $XT_{0,\pm1} = -34.5$ dB at $\lambda = 1.55$ μm. Similarly, when $\alpha = +120°$ (or $\alpha = -120°$), Rx^{+1} (or Rx^{-1}) receives maximum radiated power with an $IL = 8.5$ dB and the worst-case crosstalk is $XT_{\pm1,0} = -24.4$ dB. Figures 8 (b), (d) and (f) show the electric field profiles $|E|$ for different phase shifts between the OPAs elements. The oscillations visible in the field pattern are the consequence of constructive and destructive interference due to multiple reflections arising from the material discontinuities in the multilayer configuration.

In Fig. 9, we report a comparison of the electric field distribution in the $XZ-$plane (i.e., elevation plane when $\phi = 0°$) for the channel link assuming a homogeneous host medium (a), and an on-chip multilayer structure (b). The field profiles are plotted at $\lambda = 1.55$ μm by considering the transmitter pointing towards the broadside receiver. The results show that, when the link is hosted in an infinite homogeneous medium, the field scatters as it propagates along the channel (Fig. 9 (a)), while in
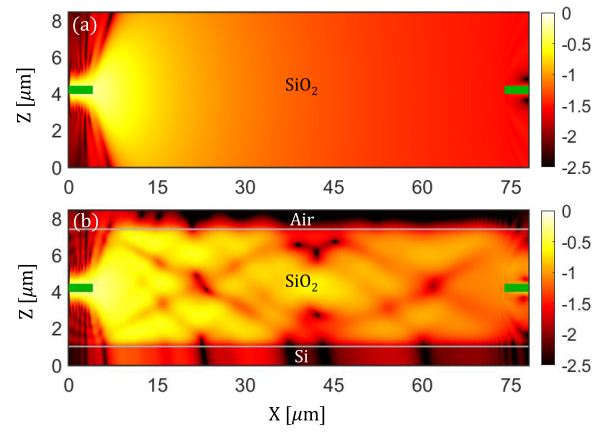

Fig. 9. A comparison of the electric field $|E|$ profile (in log scale) of the optical link in the $XZ-$plane at $\lambda = 1.55$ μm, considering the broadside communication in (a) an infinite homogeneous host medium and (b) the multilayer design with multipath propagation effect.
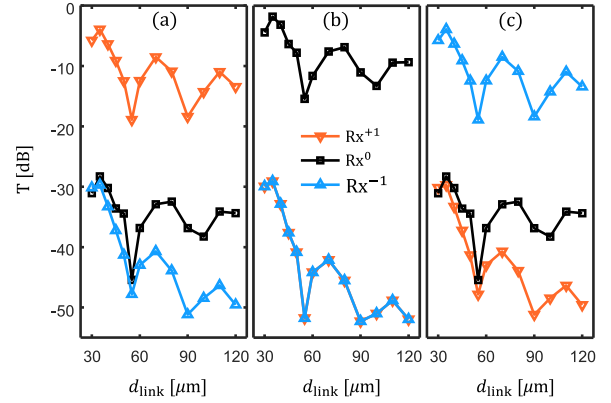

Fig. 10. Transmittance in dB at each receiving node as a function of the link distance d_{link} considering $h_c = 3$ μm. Each transmitting and receiving OPA is made up of $N_a = 3$ elements. The phase difference between the radiators of the OPAs is (a) $\alpha = -120°$, (b) $\alpha = 0°$ and (c) $\alpha = +120°$.

the case of a multilayer structure the field is confined between the lower Si and upper air layers (Fig. 9 (b)). This sort of confined propagation, consequently, leads to received signals with higher strength as compared to infinite homogeneous embedding medium.

The link distance and thickness of the cladding layer are design parameters that can be exploited to improve the device performance. The transmittance at each receiving OPA as a function of link distance d_{link} is plotted in Fig. 10. By considering communication with the central node Rx^0, the maximum transmission is observed at $d_{\text{link}} = 35$ μm with an insertion loss $IL = 1.8$ dB and crosstalk $XT_{0,\pm1} = -27.28$ dB. For the steered beam ($\alpha = \pm120°$), the best-case insertion loss is $IL = 3.93$ dB and the worst-case crosstalk is $XT_{\pm1,0} = -24.36$ dB. The effect of link distance can be easily understood as changing the d_{link} means either bringing the receivers closer to or moving them away from the transmitter, which can place them at interference minima or maxima, as shown in Fig. 9 (b). These results show that the link distance is a crucial parameter in the design criteria and must be carefully chosen as it has a strong influence on the received signal.

The thickness of the cladding layer is another important parameter which can affect the performance of the device. It provides an extra degree of freedom to optimize the device

performance. The other layers can also play their role, but their thickness is constrained by the commercial wafers, thus making difficult to vary their thicknesses. Therefore, in the present analysis, we study the impact of the thickness of the cladding layer on the device performance. Figure 11 shows the transmittance computed as a function of thickness of cladding layer h_c at $d_{link} = 35$ μm. It can be observed that h_c has a considerable impact on the received power. In the present setup, we observe maximum transmittance at $h_c = 3$ μm and a minimum transmittance at $h_c = 4$ μm. In fact, the change in the cladding thickness influences the condition for constructive and destructive interference. For a fixed link distance, the thickness of the cladding layer can be carefully chosen to enhance the device performance. The parameter h_c, therefore, provides an extra degree of freedom to optimally design the switching device.

We also analyze the performance of the optical link based on the OPAs with $N_a = 5$ LN taper antennas. As discussed in Section II-B, by considering the radiation diagram in Fig. 5 (b), it is possible to exploit the OPAs with $N_a = 5$, to implement a 1×5 on-chip wireless switch. Nevertheless, for the sake of brevity and to streamline the discussion, we consider exactly the same scenario of 1×3 switch as discussed previously, with the only difference being that each OPA now has $N_a = 5$ antennas. The separation between two adjacent elements of the OPAs is the same as considered previously, i.e., $d_a \approx \lambda_m$ (λ_m being the wavelength in the cladding medium SiO_2). The phase shift required for an efficient beam steering to address the side receivers is $\alpha = \pm 360°/N_a = \pm 72°$. The transmittance calculated at each receiving OPA at the free-space wavelength $\lambda = 1.55$ μm is plotted in Fig. 12. The broadside receiver has an IL $= 0.83$ dB and $XT_{0,\pm 1} = -24$ dB at $d_{link} = 80$ μm, whereas, the side receivers have the best-case IL $= 1.55$ dB and the worst-case $XT_{\pm 1,0} = -27$ dB at $d_{link} = 70$ μm. The results demonstrate that by using the OPAs with $N_a = 5$, the received signal is relatively higher at both the broadside receiver (Rx^0) and the side receivers ($Rx^{\pm 1}$), as compared to the case of the OPAs with $N_a = 3$.

IV. FABRICATION IMPERFECTIONS: A STATISTICAL ANALYSIS

So far, we have investigated the performance of the on-chip wireless switch by considering ideal fabrication conditions, and demonstrated how the design of the OPAs and their surrounding environment can be leveraged to enhance the received power. However, the imperfections in fabrication and integration of the LN OPAs can affect their beam shaping and steering capabilities, which can consequently change the overall performance of the device. LN is a versatile material, thanks to its unique crystal structure; nevertheless precise manufacturing of LN components can present several challenges and demands a careful handling and a good understanding throughout the fabrication steps due to complex nature of the etching processes involved. The fabrication imperfections may include the waveguide width variation, asymmetric and incorrect sidewall angles, non-uniform spacing between the antenna elements, phase shift errors, inaccuracy in the excitation amplitude, inter-component integration issues, etc.
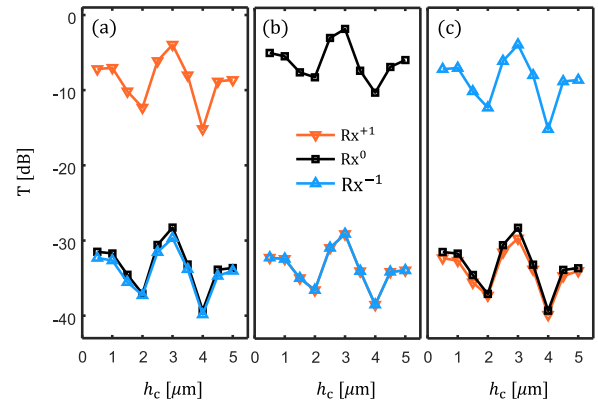

Fig. 11. Transmittance in dB at different receivers as a function of thickness of the cladding layer h_c at $\lambda = 1.55$ μm. The phase difference between the antennas of the OPAs is (a) $\alpha = +120°$, (b) $\alpha = 0°$ and (c) $\alpha = -120°$. The link distance between the transmitter and receiver is $d_{link} = 35$ μm.
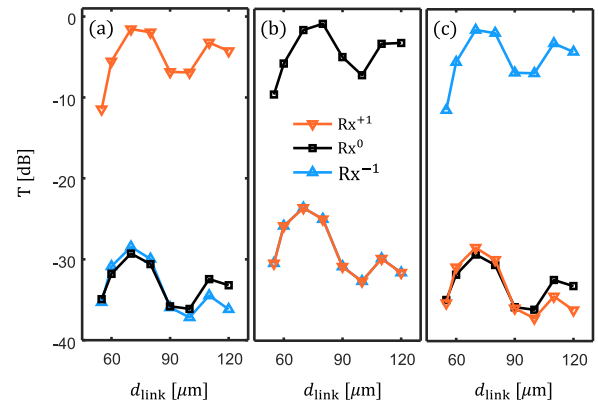

Fig. 12. Transmittance in dB at each receiving node as a function of the link distance d_{link} at $\lambda = 1.55$ μm. We consider that each OPA is composed of $N_a = 5$ LN taper antennas. The phase difference between the radiators of the OPAs is (a) $\alpha = +72°$, (b) $\alpha = 0°$ and (c) $\alpha = -72°$.

In this section, therefore, we present a statistical analysis of the effect of fabrication imperfections on the performance of the OPAs and the on-chip wireless switch. As an illustrative example, we consider here the case of 1×3 on-chip switch with OPAs made of $N_a = 3$ LN taper antennas. In order to do so, we numerically examine the radiation characteristics of the OPA for 500 possible realizations by randomly considering fabrication imperfections deviating from the ideal conditions. In particular, we consider random variations in the excitation amplitudes, with the mean value at $b_q = 1$, and in the input phase, with the mean value at $\alpha = 0°$, each with a standard deviation of 0.1. We denote the errors in the excitation amplitude by b_{qe} and in the phase shift by α_e. The phase errors may occur from the imperfect etching of the LN waveguides (including mismatches in waveguide size, roughness and sidewall angles) or can be due to fabrication imperfection of the phase shifters. The amplitude error can originate if the power splitters are not perfectly symmetric, and they deliver power with different splitting ratio to the input antennas. Since the phase shifters in LN usually exploit the EO effect, the phase error can be compensated by tuning the driving voltages of phase shifters. The amplitude error, on the other hand, could be relatively more difficult to mitigate. However, one possible strategy that could be used to compensate for this error is the post-fabrication tuning method, in which the device parameters are tuned after the fabrication, or by using the improved
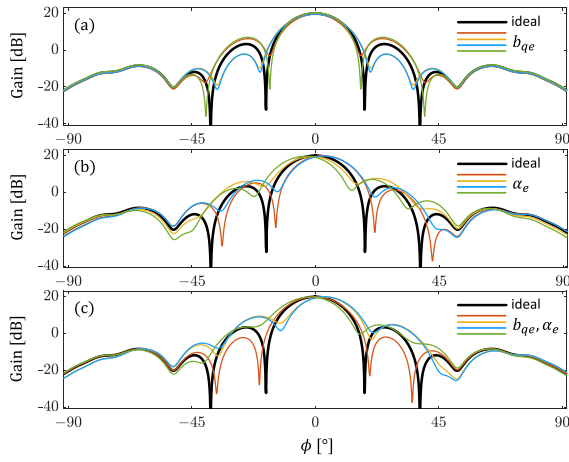
Fig. 13. Effect of fabrication imperfections on the radiation pattern of the OPA made of $N_a = 3$ LN antennas. Gain of the OPA as a function of azimuthal angle ϕ when considering fabrication errors in (a) the excitation amplitude b_{qe}, (b) the phase shift α_e, and (c) taking both variations simultaneously (b_{qe}, α_e). The thick black line illustrates the ideal scenario, while each of the remaining plots represents a radiation diagram corresponding to one of the arbitrarily chosen realization among the set of 500 possible realizations we have considered.
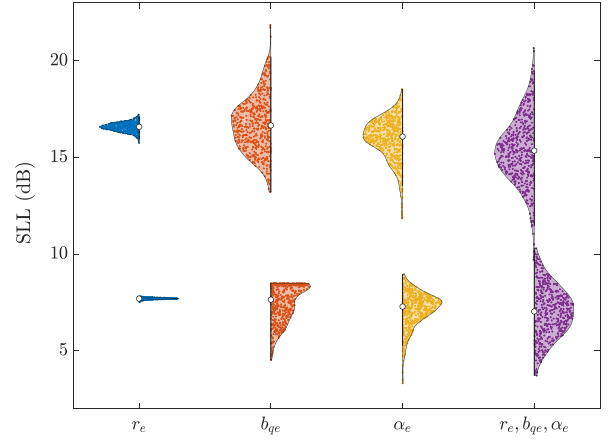

Fig. 14. Impact of fabrication imperfection on the sidelobe level (SLL) of the radiation diagram of the OPA. The radiation diagram with ideal parameters is given in Fig. 5 (a). The right half of the violin plot represents the changes in the SLL for $\alpha = 0°$, whereas, the left half represents the SLL when $\alpha = +120°$. The white circle at the center of each violin point indicates the median value of the considered samples. The plots illustrate results for the random variations in the antenna distance r_e, the excitation amplitude b_{qe}, the input phase α_e, and their combined effect.

fabrication processes, for example. The radiation diagram of the OPA under ideal fabrication conditions is presented in Fig. 5 (a). Moreover, we conduct 3-D simulations to analyse the performance of an on-chip optical switch by considering the worst-case scenario of fabrication imperfections.

Figure 13 shows the radiation diagrams of the OPA for random realizations of the fabrications errors in the excitation amplitude, input phase shift, and their combined effect. Initially, we consider random errors only in the excitation amplitude, while keeping the other parameters fixed to their ideal values. Figure 13 (a) depicts the effect of the errors in the excitation amplitude b_{qe} on the radiation diagram of the OPA with $N_a = 3$. The thick black line represents the radiation pattern in the ideal fabrication conditions (as reported in Fig. 5 (a)), whereas, each of the remaining line plot depicts a radiation diagram corresponding to one of the arbitrarily chosen realization among the set of 500 possible realizations we have considered in our analysis. We observe that the imperfections in the excitation amplitudes of the radiators primarily change the sidelobe level and the positions of the radiation minima. The sidelobe level (SLL) can be defined as the difference in dB between the maximum value of the main beam and the maximum value of the first sidelobe in the radiation diagram. The main lobe is almost unaffected by b_{qe} and the overall profile of the radiation pattern is also preserved. In addition, Fig. 13 (b) shows the OPA radiation diagrams calculated considering imperfections only in the phase shift α_e applied at each emitter of the OPA. The results show that the errors in the input phase displace the entire radiation diagram and with a stronger impact on the sidelobe level. Figure 13 (c) depicts the radiation diagram of the OPA by simultaneously taking into account the fabrication errors both in the excitation amplitudes b_{qe} and in the input phase α_e. We notice that the contemporary random variation of both the parameters b_{qe} and α_e has a more pronounced impact on the sidelobe level.

Therefore, we consider the statistical analysis of the influence of fabrication imperfections on the sidelobe level by

arbitrarily selecting 500 possible realizations. In this analysis, we take into account also the deviation in the distance between the antenna elements of the OPAs relative to the wavelength in the cladding medium. We define the ratio between the antenna distance d_a and wavelength λ_m as $r = d_a/\lambda_m$ and denote the corresponding fabrication error as r_e. We consider the variations in the antenna distance with the mean value at $r = 1.08$ and a standard deviation of 0.01. Figure 14 illustrates the sidelobe level (SLL) of the radiated beam using violin plots, considering fabrication imperfections in various parameters individually and their combined effect simultaneously. In particular, we investigate the deviation in the antenna distance r_e, the excitation amplitude b_{qe}, the phase shift α_e, and their combined effect. The data in Fig. 14 are plotted around the median value of the considered samples denoted by a white circle in the center of each violin (i.e. the coloured areas in Fig. 14), and each point on the violin represents a possible realization due to fabrication imperfections. The left half of each violin represents the variations in the SLL when $\alpha = 0°$, i.e., all emitters are in phase, while the right half represents the change in sidelobe level for the steered beam ($\alpha = +120°$). The effect of r_e on the SLL is relatively small, particularly for the SLL of the steered beam ($\alpha = +120°$). b_{qe} and α_e may have a significant impact on the SLL of both the broadside and steered beams. Furthermore, we see that considering simultaneously all the presently examined fabrication imperfections, the SLL can fluctuate up to ± 5 dB as compared to the one with the ideal parameters.

The performance of the on-chip wireless switch is then evaluated taking into account the combined effect of fabrication errors in the worst-case scenario selected from the 500 different realizations. We consider an OPA made of $N_a = 3$ antenna elements, when the fabrication error in the excitation amplitude and in the input phase of each radiator are $b_{qe} = [-0.06, -0.18, 0.22]$ and $\alpha_e = [8.85°, -8.02°, 8.47°]$, respectively. We perform numerical simulations to analyze the impact of fabrication errors on the performance of 1×3
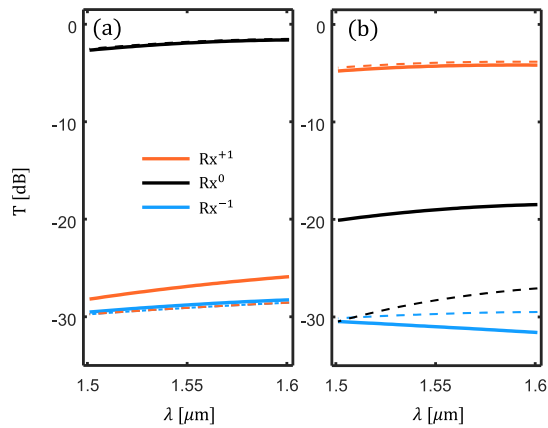
Fig. 15. Transmittance (T) as a function of input wavelength λ calculated at each receiver for (a) $\alpha = 0° + \alpha_e$ and (b) $\alpha = 120° + \alpha_e$. The dashed lines refer to the transmittance when all the parameters are taken with their ideal values, i.e., no fabrication imperfections. These results are obtained considering $h_c = 3~\mu$m and $d_{\text{link}} = 35~\mu$m.

on-chip switch in the multilayer configuration for $h_c = 3~\mu$m and $d_{\text{link}} = 35~\mu$m. The transmittance at the three receivers are plotted in in Fig. 15, when the transmitter addresses the broadside Rx^0 (Fig. 15 (a)) or the side receiver Rx^{+1} (Fig. 15 (b)). To facilitate the comparison, we also include the results for the ideal case (without any fabrication imperfection), represented by the dashed lines. As depicted in Fig. 15 (a), the transmittance calculated at each output OPA indicates that the insertion loss is IL = 1.92 dB for the broadside receiver, which is almost unaffected by the fabrication errors (b_{qe} and α_e). The crosstalk $XT_{0,+1} = -24.36$ is approximately 2 to 3 dB higher as compared to the ideal case in the considered wavelength range. For the side receiver, the insertion loss (IL = 4.27 dB) is nearly identical, but the crosstalk ($XT_{+1,0} = -14.73$ dB) is 9.28 dB higher than in the ideal scenario.

From the above-given analysis, we perceive that the performance of the wireless switch is quite robust, particularly in the context of broadside communication. The variation intervals we have considered are quite large which, in general, are conservative with respect to the actual errors occurring during the fabrication. We have shown that even considering the largest fabrication error, already taken into account in our analysis, the device performance is barely affected (see Fig. 15). Even if there is an increase in the crosstalk while addressing the side receivers, we expect an improvement in the performance when faced with the real-world fabrication imperfections, given that we are considering the worst-case scenario. Moreover, we would like to remark that the fabrication errors and the quality of the fabricated device depend on the available facilities and the optimization of the fabrication process.

V. CONCLUSION

In this work, we have investigated an on-chip optical wireless switch exploiting the integrated optical phased arrays based on the LNOI technology. We have reported the design and radiation characteristics of LN antenna element comprising the OPAs, and a parametric analysis. As an example, we have shown the results of a 1×3 on-chip optical wireless switch considering both a hypothetical infinite homogeneous

medium and a realistic multilayer structure design, exhibiting the multipath propagation phenomenon. The interconnection between transmitter and different receiving nodes can be achieved by steering the radiation beam via phase difference between the radiant elements. In addition, we have investigated how the received power is influenced by the change in geometrical parameters and the number of radiating elements of the OPAs. We show that a well-thought-out structure design with optimized parameters can provide an enhanced power at the receiving nodes. We have examined here a 1×3 wireless switch, however, in general, the OPAs can be assembled together to form $N \times N$ reconfigurable switching matrices. Thus, LNOI can be a good candidate for implementing the optical wireless switches as they can be integrated with on-chip networks as a promising alternative to microring resonator based optical systems.

REFERENCES

[1] J. He, T. Dong, and Y. Xu, "Review of photonic integrated optical phased arrays for space optical communication," *IEEE Access*, vol. 8, pp. 188284–188298, 2020.

[2] S. Liverman et al., "Dynamic indoor free-space optical communication enabled by beam steering and beam shaping," *Appl. Opt.*, vol. 62, no. 9, p. 2367, Mar. 2023.

[3] J. W. Silverstone et al., "On-chip quantum interference between silicon photon-pair sources," *Nat. Photon.*, vol. 8, no. 2, pp. 104–108, Feb. 2014.

[4] E. Lomonte et al., "Single-photon detection and cryogenic reconfigurability in lithium niobate nanophotonic circuits," *Nature Commun.*, vol. 12, no. 1, p. 6847, Nov. 2021.

[5] C.-P. Hsu et al., "A review and perspective on optical phased array for automotive LiDAR," *IEEE J. Sel. Topics Quantum Electron.*, vol. 27, no. 1, pp. 1–16, Jan. 2021.

[6] M. J. R. Heck, "Highly integrated optical phased arrays: Photonic integrated circuits for optical beam shaping and beam steering," *Nanophotonics*, vol. 6, no. 1, pp. 93–107, Jan. 2017.

[7] B. Abiri, R. Fatemi, and A. Hajimiri, "A 1-D heterodyne lens-free optical phased array camera with reference phase shifting," *IEEE Photon. J.*, vol. 10, no. 5, pp. 1–12, Oct. 2018.

[8] S.-M. Kim, E.-S. Lee, K.-W. Chun, J. Jin, and M.-C. Oh, "Compact solid-state optical phased array beam scanners based on polymeric photonic integrated circuits," *Sci. Rep.*, vol. 11, no. 1, p. 10576, May 2021.

[9] J. Notaros, "Integrated optical phased arrays: LiDAR, AR displays, biophotonics, and beyond," in *Proc. Photon. North (PN)*, Jun. 2023, pp. 1–2.

[10] Y. Guo, Y. Guo, C. Li, H. Zhang, X. Zhou, and L. Zhang, "Integrated optical phased arrays for beam forming and steering," *Appl. Sci.*, vol. 11, no. 9, p. 4017, Apr. 2021.

[11] S. A. Miller et al., "Large-scale optical phased array using a low-power multi-pass silicon photonic platform," *Optica*, vol. 7, no. 1, pp. 3–6, Jan. 2020.

[12] G. Calò et al., "Design of reconfigurable on-chip wireless interconnections through optical phased arrays," *Opt. Exp.*, vol. 29, no. 20, p. 31212, Sep. 2021.

[13] M. Chalupnik, A. Singh, J. Leatham, M. Loncar, and M. Soltani, "Scalable and ultralow power silicon photonic two-dimensional phased array," *APL Photon.*, vol. 8, no. 5, May 2023, Art. no. 051305.

[14] H. Sun, Q. Qiao, Q. Guan, and G. Zhou, "Silicon photonic phase shifters and their applications: A review," *Micromachines*, vol. 13, no. 9, p. 1509, Sep. 2022.

[15] S. Liu et al., "Thermo-optic phase shifters based on silicon-on-insulator platform: State-of-the-art and a review," *Frontiers Optoelectronics*, vol. 15, no. 1, p. 9, Apr. 2022.

[16] A. Maeder, F. Kaufmann, D. Pohl, J. Kellner, and R. Grange, "High-bandwidth thermo-optic phase shifters for lithium niobate-on-insulator photonic integrated circuits," *Opt. Lett.*, vol. 47, no. 17, p. 4375, Sep. 2022.

[17] X. Chen, J. Lin, and K. Wang, "A review of silicon-based integrated optical switches," *Laser Photon. Rev.*, vol. 17, no. 4, Apr. 2023, Art. no. 2200571.

[18] A. Prencipe and K. Gallo, "Electro- and thermo-optics response of X-cut thin film LiNbO₃ waveguides," *IEEE J. Quantum Electron.*, vol. 59, no. 3, pp. 1–8, Jan. 2023.

[19] G. Calò et al., "4 × 4 integrated switches based on on-chip wireless connection through optical phased arrays," *Photonics*, vol. 10, no. 4, p. 367, Mar. 2023.

[20] S. Werner, J. Navaridas, and M. Luján, "A survey on optical network-on-chip architectures," *ACM Comput. Surveys*, vol. 50, no. 6, pp. 1–37, Dec. 2017.

[21] F. Fuschini et al., "Multi-level analysis of on-chip optical wireless links," *Appl. Sci.*, vol. 10, no. 1, p. 196, Dec. 2019.

[22] J. Nanni et al., "Multi-path propagation in on-chip optical wireless links," *IEEE Photon. Technol. Lett.*, vol. 32, no. 17, pp. 1101–1104, Sep. 2020.

[23] F. Lemic et al., "Survey on terahertz nanocommunication and networking: A top-down perspective," *IEEE J. Sel. Areas Commun.*, vol. 39, no. 6, pp. 1506–1543, Jun. 2021.

[24] M. F. Imani, S. Abadal, and P. del Hougne, "Metasurface-programmable wireless network-on-chip," *Adv. Sci.*, vol. 9, no. 26, Sep. 2022, Art. no. 2201458.

[25] C. Garcìa-Meca et al., "On-chip wireless silicon photonics: From reconfigurable interconnects to lab-on-chip devices," *Light, Sci. Appl.*, vol. 6, no. 9, Mar. 2017, Art. no. e17053.

[26] C. V. Poulton et al., "Long-range LiDAR and free-space data communication with high-performance optical phased arrays," *IEEE J. Sel. Topics Quantum Electron.*, vol. 25, no. 5, pp. 1–8, Sep. 2019.

[27] J. Sun, E. Timurdogan, A. Yaacobi, E. S. Hosseini, and M. R. Watts, "Large-scale nanophotonic phased array," *Nature*, vol. 493, no. 7431, pp. 195–199, Jan. 2013.

[28] B. Dagens et al., "Direct observation of optical field phase carving in the vicinity of plasmonic metasurfaces," *Nano Lett.*, vol. 16, no. 7, pp. 4014–4018, Jul. 2016.

[29] C. Pin et al., "Seven at one blow: Particle cluster stability in a single plasmonic trap on a silicon waveguide," *ACS Photon.*, vol. 7, no. 8, pp. 1942–1949, Aug. 2020.

[30] W. Bogaerts and S. Selvaraja, "Silicon-on-insulator (SOI) technology for photonic integrated circuits (PICs)," in *Silicon-On-Insulator (SOI) Technology*, O. Kononchuk and B.-Y. Nguyen, Eds. Sawston, U.K.: Woodhead Publishing, 2014, pp. 395–434.

[31] C. V. Poulton et al., "Large-scale silicon nitride nanophotonic phased arrays at infrared and visible wavelengths," *Opt. Lett.*, vol. 42, no. 1, pp. 21–24, Jan. 2017.

[32] P. Wang et al., "Design and fabrication of a SiN-Si dual-layer optical phased array chip," *Photon. Res.*, vol. 8, no. 6, p. 912, Jun. 2020.

[33] M. Zhang, C. Wang, P. Kharel, D. Zhu, and M. Lončar, "Integrated lithium niobate electro-optic modulators: When performance meets scalability," *Optica*, vol. 8, no. 5, p. 652, May 2021.

[34] R. Luo, Y. He, H. Liang, M. Li, and Q. Lin, "Highly tunable efficient second-harmonic generation in a lithium niobate nanophotonic waveguide," *Optica*, vol. 5, no. 8, pp. 1006–1011, Aug. 2018.

[35] I. Krasnokutska, J.-L. J. Tambasco, X. Li, and A. Peruzzo, "Ultra-low loss photonic circuits in lithium niobate on insulator," *Opt. Exp.*, vol. 26, no. 2, pp. 897–904, 2018.

[36] Z. Vakulov et al., "Piezoelectric energy harvester based on LiNbO₃ thin films," *Materials*, vol. 13, no. 18, p. 3984, Sep. 2020.

[37] C. Wang et al., "Integrated lithium niobate electro-optic modulators operating at CMOS-compatible voltages," *Nature*, vol. 562, no. 7725, pp. 101–104, 7725.

[38] H. Abediasl and H. Hashemi, "Monolithic optical phased-array transceiver in a standard SOI CMOS process," *Opt. Exp.*, vol. 23, no. 5, p. 6509, Mar. 2015.

[39] S. Chung, H. Abediasl, and H. Hashemi, "A monolithically integrated large-scale optical phased array in silicon-on-insulator CMOS," *IEEE J. Solid-State Circuits*, vol. 53, no. 1, pp. 275–296, Jan. 2018.

[40] Y. Thonnart et al., "POPSTAR: A robust modular optical NoC architecture for chiplet-based 3D integrated systems," in *Proc. Design, Autom. Test Eur. Conf. Exhib. (DATE)*, Mar. 2020, pp. 1456–1461.

[41] S. Saravi, T. Pertsch, and F. Setzpfandt, "Lithium niobate on insulator: An emerging platform for integrated quantum photonics," *Adv. Opt. Mater.*, vol. 9, no. 22, Nov. 2021, Art. no. 2100789.

[42] G. Yue and Y. Li, "Integrated lithium niobate optical phased array for two-dimensional beam steering," *Opt. Lett.*, vol. 48, no. 14, p. 3633, Jul. 2023.

[43] F. Arab Juneghani et al., "Thin-film lithium niobate optical modulators with an extrapolated bandwidth of 170 GHz," *Adv. Photon. Res.*, vol. 4, no. 1, Jan. 2023, Art. no. 2200216.

[44] R. Gao et al., "Lithium niobate microring with ultra-high Q factor above 108," *Chin. Opt. Lett.*, vol. 20, no. 1, 2022, Art. no. 011902.

[45] R. Gao et al., "Broadband highly efficient nonlinear optical processes in on-chip integrated lithium niobate microdisk resonators of Q-factor above 108," *New J. Phys.*, vol. 23, no. 12, Dec. 2021, Art. no. 123027.

[46] D.-Y. Guo, J.-M. Liu, and D.-L. Zhang, "LNOI photonic wire switch based on phase transition material," *Opt. Laser Technol.*, vol. 150, Jun. 2022, Art. no. 107972.

[47] W. Li et al., "High-speed 2D beam steering based on a thin-film lithium niobate optical phased array with a large field of view," *Photon. Res.*, vol. 11, no. 11, p. 1912, Nov. 2023.

[48] Z. Wang et al., "Fast-speed and low-power-consumption optical phased array based on thin-film lithium niobate platform," 2023, *arXiv:2304.11591*.

[49] Y. Li et al., "Design of optical phased array with low-sidelobe beam steering in thin film lithium niobate," *Opt. Laser Technol.*, vol. 171, Apr. 2024, Art. no. 110432.

[50] Q. Cheng, S. Rumley, M. Bahadori, and K. Bergman, "Photonic switching in high performance datacenters [invited]," *Opt. Exp.*, vol. 26, no. 12, p. 16022, Jun. 2018.

[51] X. Xue and N. Calabretta, "Nanosecond optical switching and control system for data center networks," *Nature Commun.*, vol. 13, no. 1, p. 2257, Apr. 2022.

[52] W. Yue, Y. Cai, and M. Yu, "Review of 2 × 2 silicon photonic switches," *Photon.*, vol. 10, no. 5, 2023.

[53] G. Ulliac, V. Calero, A. Ndao, F. Baida, and M.-P. Bernal, "Argon plasma inductively coupled plasma reactive ion etching study for smooth sidewall thin film lithium niobate waveguide application," *Opt. Mater.*, vol. 53, pp. 1–5, Jan. 2016.

[54] *Ansys Lumerical FDTD | Simulation for Photonic Components*. Accessed: May 11, 2024. [Online]. Available: https://eur03.safelinks. protection.outlook.com/?url=https%3A%2F%2Fwww.ansys.com%2 Fproducts%2Foptics%2Ffdtd&data=05%7C02%7Cmuhammad.khalid% 40poliba.it%7C52a8de8450074e7eec7508dc71862e90%7C5b406aaba 1f14f13a7aadd573da3d332%7C0%7C0%7C638510068324553169% 7CUnknown%7CTWFpbGZsb3d8eyJWIjoiMC4wLjAwMDAiLCJQIjoi V2luMzIiLCJBTiI6Ik1haWwiLCJXVCI6Mn0%3D%7C0%7C%7C% 7C&sdata=IGkTtEQ0VxWxRfwFQUOq0CwlbqN3uL4JSPx%2BB hTAvF4%3D&reserved=0

[55] R. E. Collin, *Antennas and Radiowave Propagation*. New York, NY, USA: McGraw-Hill, 1985.

[56] G. Calò et al., "Reconfigurable optical wireless switches for on-chip interconnection," *IEEE J. Quantum Electron.*, vol. 59, no. 3, pp. 1–10, Jan. 2023.

[57] D. Pohl et al., "100-GBd waveguide Bragg grating modulator in thin-film lithium niobate," *IEEE Photon. Technol. Lett.*, vol. 33, no. 2, pp. 85–88, Jan. 15, 2021.

[58] L. Song et al., "Anisotropic thermo-optic Mach–Zehnder interferometer on LNOI for polarization handling and multiplexing," *Laser Photon. Rev.*, vol. 17, no. 8, Aug. 2023, Art. no. 2300025.

[59] J. D. Kraus, *Antennas*, 2nd ed. McGraw-Hill: New York, NY, USA, 1988.

[60] D. Zhu et al., "Integrated photonics on thin-film lithium niobate," *Adv. Opt. Photon.*, vol. 13, no. 2, pp. 242–352, 2021.

Muhammad Khalid received the Ph.D. degree in electromagnetics from the "La Sapienza" University of Rome, Italy, in 2016. Following his Ph.D. studies, he was a Post-Doctoral Researcher with the Italian Institute of Technology, Arnesano, Italy, from 2017 to 2021. Subsequently, he held a post-doctoral position with Roma Tre University, Rome, Italy, from 2022 to 2023. He is currently an Assistant Professor (RTD-a) with the Department of Electrical and Information Engineering, Polytechnic University of Bari, Italy. His research interests include computational electromagnetics, metamaterials and metasurfaces, plasmonics, and nonlinear optics and photonics.

Simone Ferraresi received the bachelor's and master's degrees in electronic engineering from the University of Ferrara, Italy, in 2021 and 2024, respectively. As the coauthor of the paper, he conducted a statistical analysis of the effects of optical phased arrays (OPAs) fabrication imperfections on their performance. His research interests include silicon photonics, optical phased arrays, and optical switching.

Gaetano Bellanca received the M.Sc. degree in electronic engineering and the Ph.D. degree in electronic and computer science from the University of Bologna in 1991 and 1995, respectively. He joined the Department of Engineering, University of Ferrara, in 1999, where he is currently an Associate Professor of electromagnetics. His main research interests include the design and characterization of optical components and devices and in the development of numerical techniques for electromagnetics in the fields of applied microwave, antennas, and integrated optics.

Marina Barbiroli received the Laurea degree in electronic engineering and the Ph.D. degree in computer science and electronic engineering from the University of Bologna in 1995 and 2000, respectively. She is currently an Associate Professor with the Department of Electrical, Electronic and Information Engineering "G. Marconi," University of Bologna. Her research interests include propagation models for mobile communications systems, with a focus on wideband channel modeling for 5G systems and beyond. Her research activities include investigation of planning strategies for mobile systems, broadcast systems and broadband wireless access systems, and analysis of exposure levels generates by all wireless systems and for increasing spectrum efficiency. The research activity includes the participation to European research and cooperation programs (COST 259, COST 273 COST2100, COST IC1004, COST IRACON, and COST INTERACT) and in the European Networks of Excellence FP6-NEWCOM and FP7-NEWCOM++.

Franco Fuschini received the M.Sc. degree in telecommunication engineering and the Ph.D. degree in electronics and computer science from the University of Bologna, Italy, in March 1999 and July 2003, respectively. He is currently an Associate Professor with the Department of Electrical, Electronic and Information Engineering "Guglielmo Marconi," University of Bologna. He is the author or coauthor of more than 30 journal articles on radio propagation and wireless system design. His main research interests include radio systems design and radio propagation channel theoretical modeling and experimental investigation. He received the "Marconi Foundation Young Scientist Prize" in the context of the XXV Marconi International Fellowship Award in April 1999.

Velio Tralli (Senior Member, IEEE) received the Dr.Ing. degree (cum laude) in electronic engineering and the Ph.D. degree in electronic engineering and computer science from the University of Bologna, Italy, in 1989 and 1993, respectively. From 1994 to 1999, he was a Researcher with the National Research Council, CSITE, University of Bologna. In 1999, he joined the Department of Engineering, University of Ferrara, Italy, where he is currently an Associate Professor. He participated in several national and European research projects, and European cooperation programs addressing short-range communications systems, 3G-4G-5G wireless networks, wireless video communications, and on-chip optical wireless networks. He coauthored more than 150 articles in refereed journals, including IEEE TRANSACTIONS, and international conferences. His research interests include digital transmission and coding, and wireless communications, with an emphasis on radio resource optimization, cross-layer design, and multiantenna systems. He served as the Co-Chair for the Wireless Communication Symposium of ICC 2006 and the Communication Theory Symposium of ICC 2013. He serves as an Associate Editor for the *European Transactions on Emerging Technologies*.

Davide Bertozzi received the Ph.D. degree in electrical engineering from the University of Bologna, Italy. He has been a Visiting Researcher at international academic institutions, such as Stanford University, and major semiconductor companies, such as STMicroelectronics, NXP, Samsung, and NEC Labs America. Since 2023, he has been a Reader in advanced processing technologies with The University of Manchester, U.K. His research interests include chip-scale interconnect technology and on its capability to enable new system architectures. He is a member of the HiPEAC Network-of-Excellence on High-Performance Embedded Architectures and Compilation. In 2018, he received the Wolfgang Mehr Award from the IHP Leibniz Institute for Innovative Microelectronics, Germany, for his research in the field of silicon nanophotonic networks for 3D-stacked systems.

Vincenzo Petruzzelli was born in Bari, Italy, in 1955. He received the degree in electrical engineering from the University of Bari in 1986. He is currently a Full Professor of electromagnetics with the Department of Electrical and Information Engineering, Polytechnic University of Bari. He is a member of the Electronic Engineer Doctorate Courses. Over the years, he has dealt with various research topics, such as integrated plasmonic nanoantennas for wireless on-chip optical communications, innovative optical devices for the optical interconnects on chip, periodic structures for laser cavities based on the optical self-collimation property of mesoscopic structures, and plasmonic periodic nanostructures for the realization of plasmonic sensors. He has coauthored over 340 publications, 139 of which published on international journals and 155 presented at international conferences. He was a member of the Management Committee of the MP0805 COST Action "Novel Gain Materials and Devices Based on III-V-N Compounds." He acts as a reviewer of European and national projects.

Giovanna Calò (Member, IEEE) received the master's degree in electronic engineering and the Ph.D. degree in electromagnetics from the Polytechnic University of Bari, Bari, Italy, in 2002 and 2006, respectively. She joined the Department of Electrical and Information Engineering, Polytechnic University of Bari, in 2002, where she is currently an Associate Professor of electromagnetics. Her main research interests include computational electromagnetics, on-chip optical interconnections, integrated plasmonic nanoantennas for wireless on-chip optical communications, photonic crystals, plasmonic nanostructures, and components.